Chinese Chemical Letters 35 (2024) 109764

Contents lists available at ScienceDirect

Chinese Chemical Letters

journal homepage: www.elsevier.com/locate/cclet

3D layer-by-layer amorphous MoS_x assembled from $[Mo_3S_{13}]^{2-}$ clusters for efficient removal of tetracycline: Synergy of adsorption and photo-assisted PMS activation

Yue Li[a,b,1], Minghao Fan[a,b,1], Conghui Wang[a,b], Yanxun Li[a], Xiang Yu[a], Jun Ding[a], Lei Yan[a], Lele Qiu[a], Yongcai Zhang[c,*], Longlu Wang[d,*]

[a] School of Chemical and Printing-Dyeing Engineering, Henan International Joint Laboratory of Rare Earth Composite Materials, Henan University of Engineering, Xinzheng 451191, China
[b] School of Material Science and Engineering, Henan Polytechnic University, Jiaozuo 454001, China
[c] School of Chemistry and Chemical Engineering, Yangzhou University, Yangzhou 225009, China
[d] College of Electronic and Optical Engineering & College of Microelectronics, Institute of Flexible Electronics (Future Technology), Nanjing University of Posts & Telecommunications, Nanjing 210023, China

ARTICLE INFO

Article history:
Received 6 December 2023
Revised 20 February 2024
Accepted 11 March 2024
Available online 13 March 2024

Keywords:
Bifunctional catalyst
$[Mo_3S_{13}]^{2-}$
Adsorption
Photo-assisted PMS activation
Active sites

ABSTRACT

Peroxymonosulfate (PMS) activation and photocatalysis are effective technologies to remove organic pollutants, but the adsorption effect of the catalyst is usually unheeded in degradation process. Herein, a bifunctional catalyst of amorphous MoS_x (a-MoS_x) with 3D layer-by-layer superstructure was synthesized by assembling basic active units $[Mo_3S_{13}]^{2-}$ of MoS_2. The large interlayer spacing and high exposure of active sites render a-MoS_x to have excellent synergy of adsorption and photo-assisted PMS activation for tetracycline (TC) degradation. Experiments and DFT calculation show that TC can be efficiently enriched on a-MoS_x by pore filling, π-π interaction, hydrogen bonding and high adsorption energy. Subsequently, PMS can be quickly activated through electron transfer with a-MoS_x, resulting in high TC degradation efficiency of 96.6% within 20 min. In addition, the synergistic mechanism of adsorption and photo-assisted PMS activation was explored, and the degradation pathway of TC was expounded. This work is inspirational for constructing bifunctional catalysts with superior synergistic adsorption and catalytic capabilities to remove refractory organic pollutants in water.

World Health Organization has identified tetracycline (TC) as a key antibiotic. It is disturbing that the abuse of antibiotics poses a serious threat to ecosystems [1,2]. Generally, adsorption technology can efficiently enrich contaminants by pore-filling, hydrogen bonding, π-π interaction and electrostatic interactions [3–5]. However, by using only the adsorption technology, the pollutants cannot be degraded. Advanced oxidation processes (AOPs) based on peroxymonosulfate (PMS) activation has been applied to remove refractory organic pollutants [6–10]. When the O–O bonds of PMS break, the sulfate radicals ($SO_4^{\bullet-}$) with high oxidation potential (2.5–3.1 eV) and long half-life $t_{1/2}$ (30–40 μs) can be generated to oxidize the organic pollutants [11]. Meanwhile, further introduction of illumination to assist in activating PMS can produce more active species to improve the degradation efficiency [12–16]. Nevertheless, the contribution of pollutant adsorption by catalysts was often overlooked when using photo-assisted PMS activation to degrade contaminants. Researchers demonstrated that the adsorption process can narrow the distance between pollutants and catalysts, which is the crucial step for the PMS activation process [17]. Therefore, considering the complementarity between adsorption and photo-assistant PMS activation, the synthesis of bifunctional materials is a feasible strategy to efficiently remove antibiotics.

Recently, molybdenum disulfide (MoS_2) has been extensively investigated in the field of adsorption and PMS activation due to the typical two-dimensional sandwich structure of S-Mo-S. Li *et al.* [18] fabricated composite adsorbent of Co_3S_4–MoS_2 with a hollow structure by hydrothermal method. The good TC adsorption performance of Co_3S_4–MoS_2 mainly depended on multiple interactions caused by abundant functional groups, including surface complexation, π-π interaction and hydrophobic effect. Su *et al.* [19] prepared the MoS_2 nanosheets vertically aligned on biochar

* Corresponding authors.
E-mail addresses: zhangyc@yzu.edu.cn (Y. Zhang), wanglonglu@hnu.edu.cn (L. Wang).
[1] These authors contributed equally to this work.

https://doi.org/10.1016/j.cclet.2024.109764
1001-8417/

material, which can efficiently activate PMS. The vertical structure can expose abundant catalytic sites, accelerating the production of reactive species. Although these reported MoS_2 based composites have increased number of functional groups and active sites to improve the adsorption and catalytic capabilities, their complex preparation processes and high costs make them unpractical. In addition, the basal planes of MoS_2 are inert, resulting in the very limited adsorption and catalytic active sites [20]. Therefore, the construction of single MoS_x with bifunction by regulating the coordination environments of Mo-S bonds, which can generate maximum adsorption and catalytic sites, is a tremendous challenge.

Herein, we developed a simple oil bath heating approach to prepare a 3D layer-by-layer amorphous MoS_x (a-MoS_x) superstructure by assembling basic unit $[Mo_3S_{13}]^{2-}$ clusters. The unique channels and disordered arrangements in a-MoS_x can maximize the access to reactants and the exposure of active sites, making it an efficient bifunctional catalyst for synergy of adsorption and photo-assisted PMS activation. As a result, the prepared a-MoS_x exhibits far greater adsorption capacity (106.91 mg/g) for TC, in comparison with 1T/2H MoS_2 (47.92 mg/g). The TC adsorption mechanism of a-MoS_x was explored by several characterization methods, mainly involving pore filling, π-π interaction and hydrogen bonding. Afterwards, the synergistic degradation process was comprehensively studied by triggering the PMS system, and possible degradation pathways of TC were proposed. Moreover, density functional theory (DFT) calculations were employed to explore the adsorption energy of TC and PMS on a-MoS_x and corresponding electron transfer. In this work, the construction of bifunctional catalyst with strong adsorption and catalytic abilities provides new insights for future water treatment.

The chemicals, synthesis method, characterization, processes of adsorption and activation of PMS and DFT calculation are listed in Texts S1-S5 and Eqs. S1-S4 (Supporting information). The standard curve of TC was shown in Fig. S1 (Supporting information).

The detail preparation process of a-MoS_x was shown in Fig. S2 (Supporting information). For comparison, 1T/2H MoS_2 sample was synthesized by hydrothermal method. Fig. 1a illustrates the model of the 1T/2H MoS_2 flower-like structure. For the prepared a-MoS_x, it exhibits an obvious 3D layer-by-layer superstructure formed by assembling $[Mo_3S_{13}]^{2-}$ clusters (Fig. 1b). The unique structure has large interlayer spacing, allowing for maximized accessibility to reactants and exposing abundant active sites. For each monolayer, it is assembled of $[Mo_3S_{13}]^{2-}$ clusters (Fig. 1c). The disordered polymer chain can produce more unsaturated S ligands (show in the red arrow) to greatly increase the active sites. Fig. 1d and Fig. S3 (Supporting information) demonstrate that the synthesized 1T/2H MoS_2 sample with distinct nanoflower structure and 1T/2H mixed phases. The morphology of the prepared a-MoS_x is shown by SEM (Fig. 1e) and TEM (Fig. 1f) images. Obviously, the a-MoS_x exhibits a wormlike assembling structure, which consists of face-to-face monolayer nanosheet. The corresponding HRTEM images in Figs. 1g and h demonstrate the highly disordered feature of a-MoS_x. Notably, the lattice spacing of 0.67 nm comes from the layer-by-layer stacking domains in a-MoS_x [21]. The EDS mappings indicate that the elements of Mo and S are presented in the a-MoS_x (Fig. S4 in Supporting information). Furthermore, the Raman and XRD characterization results also confirm the successful preparation of 1T/2H MoS_2 and a-MoS_x (Fig. 1i, Fig. S5 and Text S6 in Supporting information) [21–23].

The adsorption and catalytic degradation of TC by 1T/2H MoS_2 and a-MoS_x were compared by adsorption and photo-assistant PMS activation experiments (Fig. 2a). The TC adsorption capacity (23.6%) of 1T/2H MoS_2 was mediocre and only 74.6% of TC was eliminated by photo-assistant PMS activation after 60 min. For

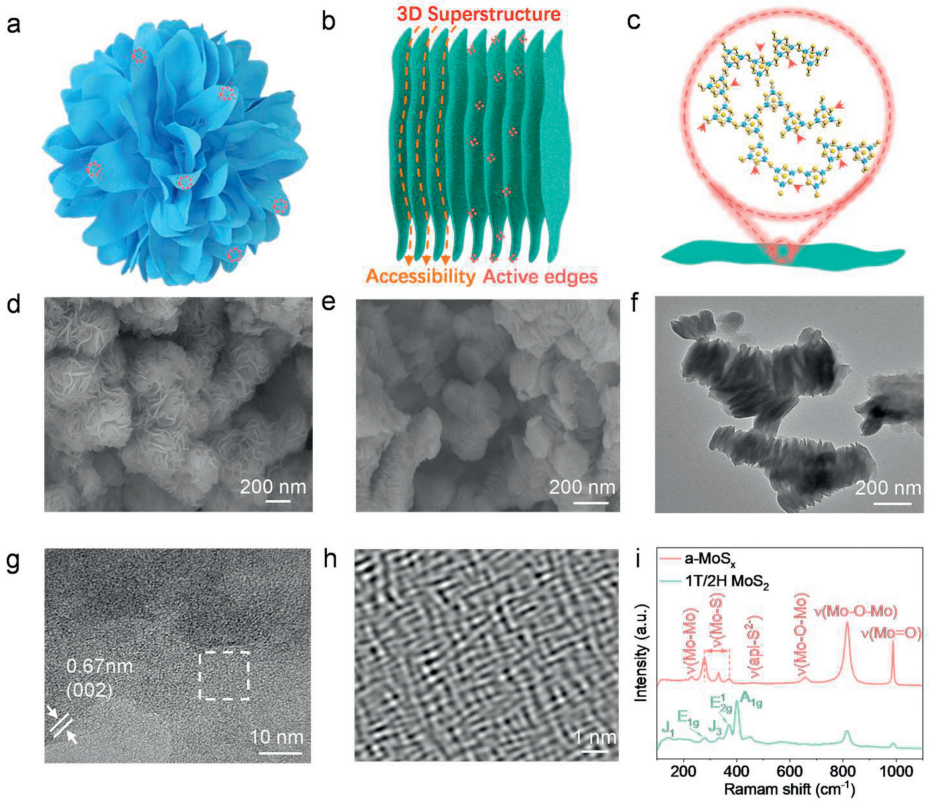

Fig. 1. Illustration of (a) 1T/2H MoS_2 nanoflower structure, (b) a-MoS_x worm-like superstructure and (c) molecular structure of monolayer a-MoS_x. SEM of (d) 1T/2H MoS_2 and (e) a-MoS_x. (f) TEM image of a-MoS_x. (g) HRTEM image of a-MoS_x and (h) magnified image of white box in (g). (i) Raman patterns of a-MoS_x and 1T/2H MoS_2.

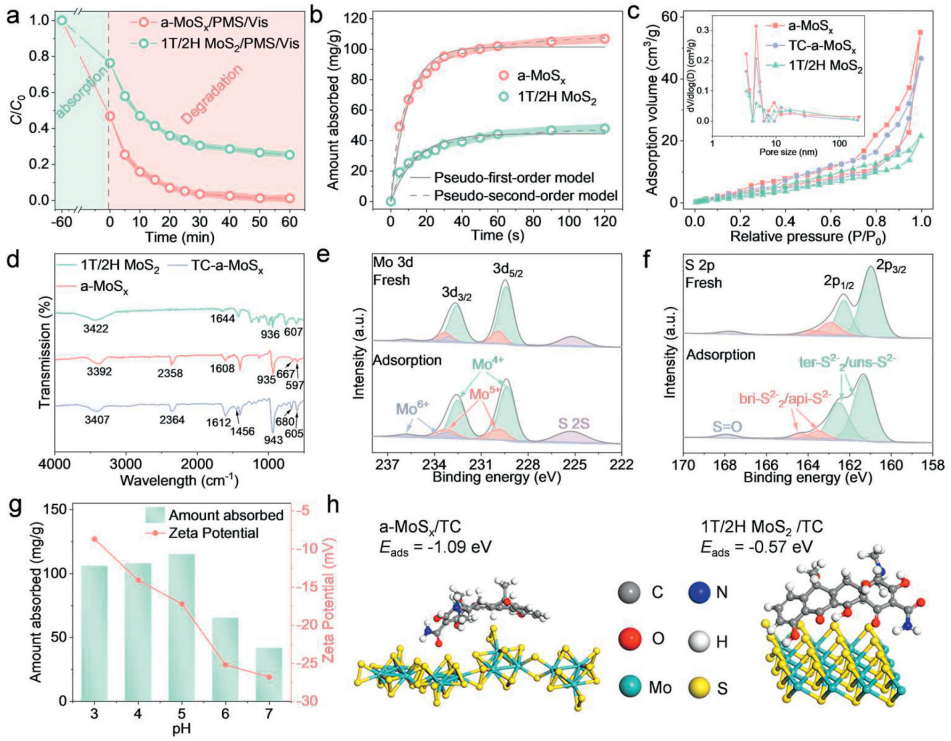

Fig. 2. (a) Adsorption and photo-assistant PMS activation curves of a-MoS_x and 1T/2H MoS_2. (b) Adsorption kinetics of different catalysts. (c) N_2 adsorption-desorption isotherms of different catalysts, inset shows the pore-size distribution curves. (d) FTIR spectra of a-MoS_x, TC-a-MoS_x (a-MoS_x after adsorption of TC) and 1T/2H MoS_2. XPS spectra of (e) Mo 3d and (f) S 2p of a-MoS_x before and after TC adsorption. (g) Zeta potentials of a-MoS_x at different pH and maximum adsorption capacity of TC. (h) Adsorption energies of TC on the surface of a-MoS_x and 2H MoS_2. Conditions: [Catalyst] = 0.050 g/L, pH 5.0, [TC] = 10 mg/L.

a-MoS_x, the adsorption capacity and removal efficiency of TC was significantly improved to 53.2% and 98.8%, respectively, which may be attributed to the larger layer spacing in a-MoS_x and the effective exposure of active sites due to the abundant unsaturated S atom. In addition, it was found that pH 5 was the optimal adsorption condition (Fig. S6 in Supporting information).

The TC adsorption capacities of 1T/2H MoS_2 and a-MoS_x were shown in Fig. 2b. It can be observed that the a-MoS_x presents a superior adsorption capacity (106.91 mg/g) compared to 1T/2H MoS_2 (47.92 mg/g). The kinetic models and the isotherms models were used to explore the adsorption process of TC. The maximum adsorption capacity and the related parameters were shown in Tables S1 and S2 in Supporting information. The adsorption process of TC is more suitably described by the *pseudo*−second−order mode and Langmuir isotherm, suggesting that chemisorption and homogeneous molecular adsorption are the dominant adsorption behavior (Fig. 2b and Fig. S7 in Supporting information) [24]. In addition, the intraparticle diffusion model find that adsorption process is related to multiple steps including film diffusion and intraparticle diffusion (Fig. S8 and Table S3 in Supporting information).

Subsequently, the Brunauer-Emmett-Teller (BET), Fourier transform infrared spectroscopy (FTIR), X-ray photoelectron spectroscopy (XPS) and zeta potential were used to further explore the adsorption mechanism. As depicted in Fig. 2c and Table S4 (Supporting information), the a-MoS_x demonstrates larger surface area, pore volume and average pore size than those of 1T/2H MoS_2, which may be attributed to the larger interlayer spacing in a-MoS_x. It should be noted that the value of pore size, pore volume and specific surface area all decrease to some extent after adsorbing TC molecule on a-MoS_x, suggesting that pore filling is one of the adsorption mechanisms [25]. Fig. 2d and Table S5 (Supporting information) show the FTIR spectra of 1T/2H MoS_2, a-MoS_x and TC adsorbed a-MoS_x (TC-a-MoS_x). It can be obviously observed that the positions of O–H, Mo=O and S-H bonds of a-MoS_x change after adsorption of TC, resulting from the formation of hydrogen bonding between a-MoS_x and TC [25,26]. In addition, the peaks of cumulated double bond, C=O and Mo-S are also shifted to some extent, suggesting that the presence of π-π stacking interaction [26,27]. Furthermore, the chemical valences of a-MoS_x and TC-a-MoS_x were investigated by XPS analysis and the related parameters were shown in Table S6 (Supporting information). In the full XPS spectra (Fig. S9a in Supporting information), the higher intensity of C 1s and O 1s were observed in TC-a-MoS_x, demonstrating that TC were successfully adsorbed on a-MoS_x [18]. In Mo 3d XPS spectrum (Fig. 2e), the area percentage of S 2s increase from 13.2% to 14.7% and the positions shift as well after loading of TC, suggesting that there may be interactions between S atoms and TC molecules [18]. Notably, in S 2p spectrum, the positions and area percentages of bridging sulfur S_2^{2-} (bri-S_2^{2-})/apical sulfur S^{2-} (api-S^{2-}) and terminal sulfur S_2^{2-} (ter-S_2^{2-})/unsaturated S^{2-} (uns-S^{2-}) also change after TC adsorption (Fig. 2f), demonstrating that the existence of π-π stacking interactions between the benzene ring of TC molecule and the outer S atoms of a-MoS_x [28]. Moreover, in C 1s spectrum (Fig. S9b in Supporting information), the peak position of C=O and C–O shift slightly after TC adsorption, illustrating that oxygen-containing groups are involved in the adsorption process between TC and a-MoS_x [28]. In O 1s spectrum (Fig. S9c in Supporting information), the peaks of C-O, H-O and Mo-O shift with amplitudes of 0.17, 0.33 and 0.12 eV and all of their area percentages also change, which may be attributed to the existence of hydrogen bonding between oxygen-containing groups in a-MoS_x and TC molecules [28]. Solution pH was a critical environmental factor to alter the species distribution of TC and surface charging state of adsorbent. As can be seen in Fig. 2g and Fig. S10 (Supporting information), there is almost no electrostatic interaction occurring between the negatively charged forms of a-MoS_x and TC at differ-

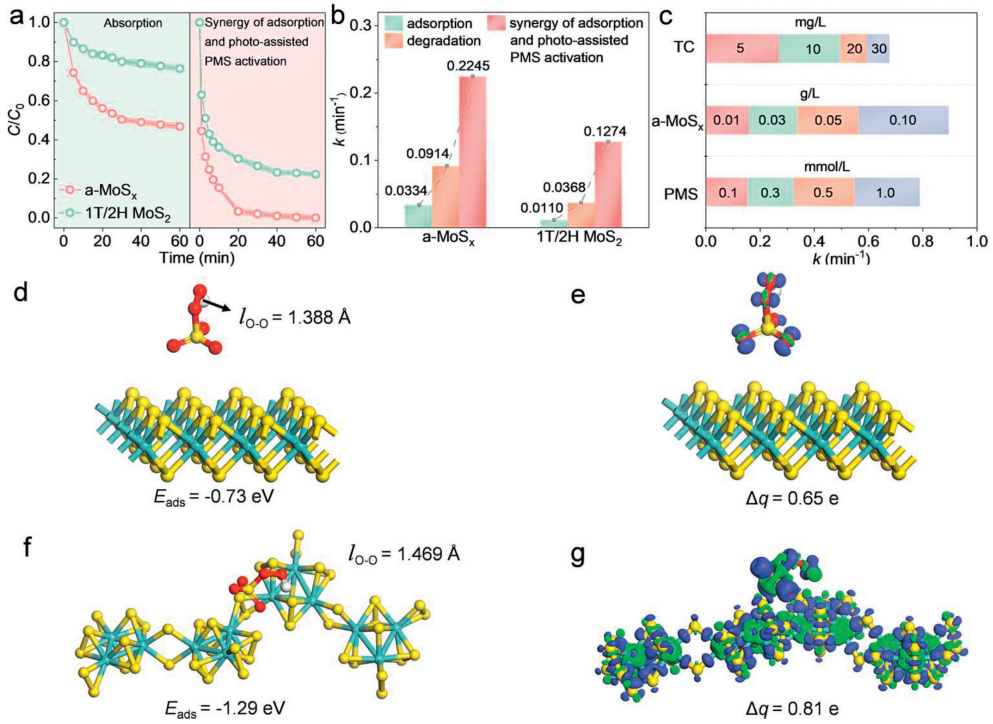

Fig. 3. (a) Performance of a-MoS_x and 1T/2H MoS_2 in the adsorption and in synergy of adsorption and photo-assistant PMS activation. (b) Comparison of rate constants *k*. (c) The reaction rate constants *k* of optimized processes. The calculated E_{ads} of PMS on (d) 2H MoS_2 and (f) a-MoS_x. The charge density difference diagrams of PMS adsorbed on (e) 2H MoS_2 and (g) a-MoS_x. The blue represents gaining electrons and the green represents losing electrons. Conditions: [Catalyst] = 0.050 g/L, pH 5.0, [PMS] = 0.5 mmol/L, [TC] = 10 mg/L.

ent pH values, suggesting that non-electrostatic interactions is the dominant driving force (the detailed information in Text S7 in Supporting information) [28]. DFT calculations were used to verify the adsorption capacity of TC on a-MoS_x (Fig. 2h). The adsorption energy of TC on a-MoS_x (−1.09 eV) is 1.91 times stronger than that on 1T/2H MoS_2 surface (−0.57 eV), demonstrating that the interaction forces and interlayer spacing presented in a-MoS_x are more conducive to the adsorption of TC. Above all, the superior adsorption capacity of a-MoS_x for TC depends on pore filling, π-π interaction, hydrogen bonding and high adsorption energy, providing strong driving forces for effective adsorption of TC.

Adsorption technology only transfers contaminants to the surface of catalyst, but cannot effectively degrade pollutants. Therefore, further exploration of synergy of adsorption and phototo-assistant PMS activation by a-MoS_x is necessary. As depicted in Fig. 3a, under the synergy of adsorption and photo-assistant PMS activation, the removal efficiency and rate constant *k* of a-MoS_x could reach 96.6% and 0.2245 min^{-1} within 20 min. These values are much higher than those of only adsorption (43.9% or 0.0334 min^{-1}) and only photo-assistant PMS activation (92.9% or 0.0914 min^{-1}) within 20 min, as shown in Fig. 3b. The faster degradation efficiency and less degradation time are beneficial to saving sewage treatment costs. Moreover, the synergy ability of a-MoS_x was obviously higher than that of 1T/2H MoS_2, which may be attributed to the presence of more active sites in a-MoS_x. To further optimize the experimental parameters, the influence of oxidant kinds, oxidant concentration, catalyst dosage and pollutant on the synergistic system was investigated (Figs. S11-S14 and Text S8 in Supporting information). Fig. 3c shows that 0.5 mmol/L PMS, 0.05 g/L a-MoS_x and 10 mg/L TC are the optimized parameters and selected for the subsequent experiments. Table S7 showed other reported bifunctional catalysts with synergistic effects of adsorption and catalysis. It could be found that our prepared a-MoS_x had excellent degradability capacity.

Theoretical calculations can be used to further explore the better activation of PMS on a-MoS_x than 1T/2H MoS_2. As presented in Figs. 3d and f, the adsorption energy of PMS on a-MoS_x surface (−1.29 eV) is stronger than that on 1T/2H MoS_2 surface (−0.73 eV). Meanwhile, the O–O bond length (l_{O-O}) of PMS (1.333 Å) is stretched to 1.388 Å for 1T/2H MoS_2 and 1.469 Å for a-MoS_x, respectively. The higher adsorption energy and longer l_{O-O} length indicate that a-MoS_x is more conducive to the dissociation of PMS. Moreover, the transfer of 0.65 and 0.81 electrons from 1T/2H MoS_2 and a-MoS_x to PMS can be seen from the charge density difference images (Figs. 3e and g), manifesting that a-MoS_x with abundant unsaturated S coordination has stronger electron transfer capacity. All the above results are consistent with excellent TC degradation efficiency of a-MoS_x.

In order to explore the valence state change and catalytic mechanism, XPS analysis of a-MoS_x before and after catalyzing TC degradation was performed (Fig. S15 in Supporting information). As shown in Fig. S15b, the amount of Mo^{4+} decreases from 69.69% to 55.38% and the contents of Mo^{5+} and Mo^{6+} increase from 17.16% to 33.19% after catalyzing TC degradation, suggesting that the existence of valence cycle of $Mo^{4+}/Mo^{5+}/Mo^{6+}$, which contributes to the activation process of PMS [29]. Fig. S15c shows that the content of S atom also decreases after catalyzing TC degradation, especially for the bri-S_2^{2-}. This indicates that more bri-S_2^{2-} are captured by H^+ in the solution, which may be due to the higher catalytic activity of bri-S_2^{2-}. In addition, the increase in S=O bond content may be due to the participation of S species with reduction ability in the regeneration process of Mo^{4+} [30]. The detail mechanism will be discussed later. A series of free radical scavenging experiments were conducted to find out the main reactive oxygen species in TC degradation process. *Tert*–butyl alcohol (TBA) and methanol (MeOH) were commonly selected as the quenching agents of $^{\bullet}OH$ and $^{\bullet}OH + SO_4^{\bullet-}$ due to the fast second-order reaction rates (TBA: $k_{\bullet OH} = 3.8–7.6 \times 10^8$ L mol^{-1} s^{-1}; MeOH:

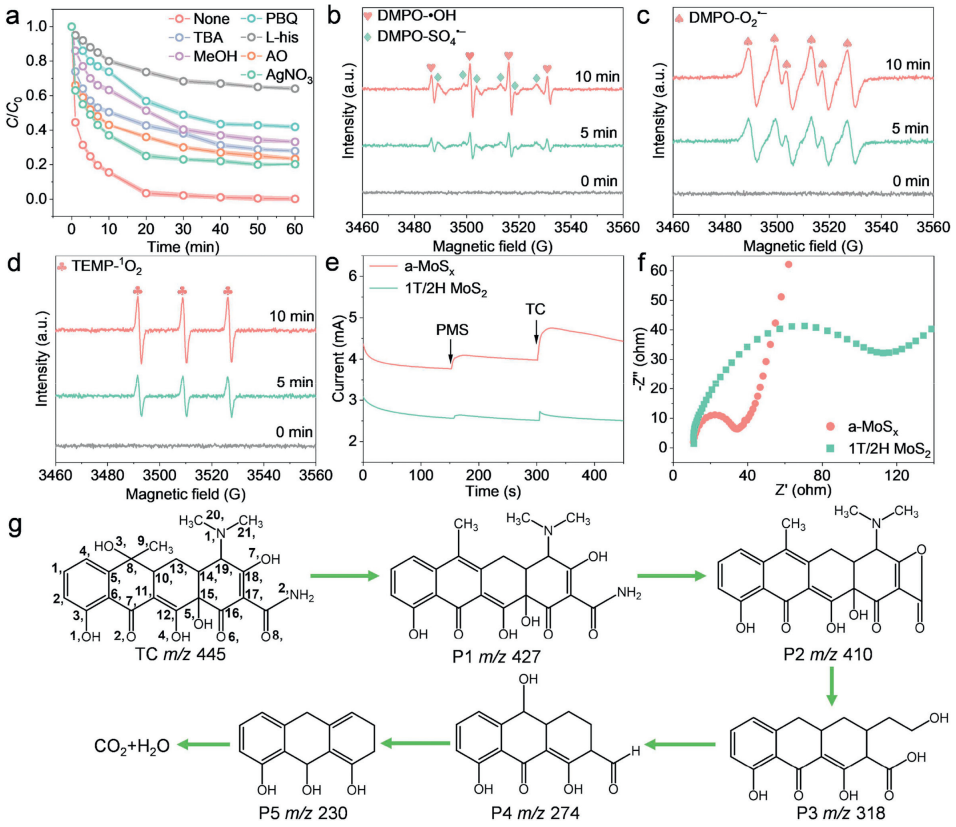

Fig. 4. (a) Effects of radical scavengers on TC degradation by a-MoS_x/PMS/light in synergistic system. EPR spectra of (b) $SO_4^{\bullet-}$ and $^{\bullet}OH$, (c) $O_2^{\bullet-}$ and (d) $^1O_2$ in synergy of adsorption and photo-assistant PMS activation by a-MoS_x. (e) *i*–*t* curves of a-MoS_x and 1T/2H MoS_2 with adding PMS and TC. (f) EIS curves of a-MoS_x and 1T/2H MoS_2. (g) Possible degradation pathway of TC by a-MoS_x/PMS/light. Conditions for (a): [a-MoS_x] = 0.050 g/L, pH 5.0, [PMS] = 0.5 mmol/L, [TC] = 10 mg/L, [TBA] = [MeOH] = 200 mmol/L, [PBQ] = [AO] = [$AgNO_3$] = 1.0 mmol/L, [L-his] = 20 mmol/L.

$k_{SO_4^{\bullet-}} = 2.5 \times 10^7$ L mol^{-1} s^{-1}, $k_{\bullet OH} = 9.7 \times 10^7$ L mol^{-1} s^{-1}) [31]. The L-histidine (L-his), *p*-benzoquinone (*p*-BQ), ammonium oxalate (AO) and $AgNO_3$ were used as scavengers for $^1O_2$, $O_2^{\bullet-}$, h^+ and e^- [32–35], respectively. The highest inhibition of TC removal at scavenger concentrations of 200 mmol/L MeOH, 200 mmol/L TBA, 1 mmol/L PBQ, 1 mmol/L AO, 1 mmol/L $AgNO_3$ and 20 mmol/ L-his were shown in Fig. S16 (Supporting information) and Fig. 4a. The TC degradation efficiency was slightly reduced to 66.8% and 72.1% after the addition of 200 mmol/L MeOH and TBA, indicating that the contribution of $^{\bullet}OH$ is higher than that of $SO_4^{\bullet-}$. The slight inhibition by AO and $AgNO_3$ manifests that h^+ and e^- contribute little to the TC degradation. On the contrary, the sluggish degradation efficiency after adding PBQ and L-his demonstrate that the dominant role of $O_2^{\bullet-}$ and $^1O_2$. EPR experiments were performed to further confirm the reactive species generated in the synergy of adsorption and photo-assistant PMS activation (Figs. 4b-d). The characteristic peaks of DMPO-$SO_4^{\bullet-}$, DMPO-$^{\bullet}OH$, DMPO-$O_2^{\bullet-}$ and TEMP-$^1O_2$ were observed after 10 min [36–40]. It can be seen that DMPO-$SO_4^{\bullet-}$ exhibits weak peak intensity, indicating the generation of a small amount of $SO_4^{\bullet-}$. Furthermore, the DMPO-$O_2^{\bullet-}$ and TEMP-$^1O_2$ display obviously stronger peak intensity than DMPO-$^{\bullet}OH$ and DMPO-$SO_4^{\bullet-}$, which demonstrates convincingly that the $O_2^{\bullet-}$ and $^1O_2$ are the main active species. Electron migration in TC degradation was analyzed by *i*–*t* curves (Fig. 4e). The current output of a-MoS_x increased much more sharply compared with that of 1T/2H MoS_2 after the introduction of PMS, indicating that more efficient electron transfer occurs from a-MoS_x to PMS. Further improvement of the current was observed after the injection of TC, manifesting that the electrons of TC are transferred to high redox potential region [41]. The smaller arc radius of a-MoS_x than 1T/2H MoS_2 in electrochemical impedance spectroscopy (EIS) curves (Fig. 4f) also indicates the faster electron transfer of a-MoS_x, which was consistent with the results of the DFT calculations [42,43].

Based on the LC-MS spectra (Fig. S17 in Supporting information), the degradation pathway of TC is proposed and presented in Fig. 4g. First, TC was transformed to product **P1** (*m/z* 427) induced by dehydration reaction on C8 site [44]. Then, **P2** (*m/z* 410) was derived from the C–N bond cleavage at N2 site [45]. Meanwhile, **P2** generated another intermediate **P3** (*m/z* 318) through the fourth ring break and -OH, -N-CH_3 and -CH_3 group removal [46]. The C18, C19 and O7 sites were attacked and the molecular chain was further broken to form **P4** (*m/z* 274) [46]. Thereafter, **P5** (*m/z* 230) formed via dihydroxylation at C8 and decarbonylation at C16 [46]. Eventually, the intermediates were further mineralized to CO_2 and H_2O. Simultaneously, the TOC removal efficiency can reach 56.8% within 30 min in synergistic system (Fig. S18 in Supporting information).

Overall, as illuminated in Fig. 5 and Text S9 (Supporting information), the degradation mechanism of TC by a-MoS_x was proposed, involving the synergy of adsorption and photo-assistant PMS activation process. For the adsorption process, due to its larger layer spacing and more interaction forces, a-MoS_x exhibits excellent adsorption performance for TC through pore filling, hydrogen bonding and π-π interactions. Simultaneously, PMS was rapidly attracted by a-MoS_x due to the stronger E_{ads} of PMS on a-MoS_x. For the photo-assistant PMS process, the numerous unsaturated S atoms in a-MoS_x combined with protons in aqueous solution to generate H_2S, resulting in the exposure of Mo^{4+}. Then, the adsorbed PMS reacted with Mo^{4+} to generate $SO_4^{\bullet-}$ and Mo^{5+}/Mo^{6+}, while Mo^{5+}/Mo^{6+} were turned back to the Mo^{4+} with the aid of

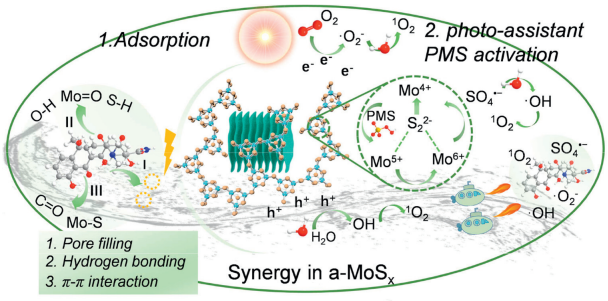

Fig. 5. Schematic diagram of the TC removal mechanism by a-MoS_x in synergy of adsorption and photo-assistant PMS activation.

PMS (Eqs. S4-S6 in Supporting information). Notably, we deduce that reduced S_2^{2-} can also react with Mo^{6+} or Mo^{5+} to promote the regeneration of metal active sites of Mo^{4+} (Eqs. S7-S10 in Supporting information). After further introduction of illumination, h^+ and e^- can be formed. O_2 in solution will react with the e^- in the conduction band to generate $O_2^{\bullet-}$ (Eq. S11 in Supporting information), while h^+ reacts with water to generate $^{\bullet}OH$ (Eq. S12 in Supporting information). $SO_4^{\bullet-}$ can also react with H_2O to produce $^{\bullet}OH$ (Eq. S13 in Supporting information). $^1O_2$ can be produced by the recombination of $^{\bullet}OH$ and the hydrolysis of $O_2^{\bullet-}$ (Eqs. S14 and S15 in Supporting information). Ultimately, both free and non-free radical pathways participate in the degradation of TC.

Finally, practical application tests were conducted to investigate the adaptability of the synergistic system of a-MoS_x/PMS/light. The influence of various anions on TC degradation is shown in Fig. S19 (Supporting information). In the presence of different concentrations of Cl^-, Br^- HCO_3^- and HPO_4^{2-}, the TC removal efficiency has only a limited drop, indicating that a-MoS_x has a strong anti-interference ability. Furthermore, humic acid (HA) was chosen to study the effect of natural organic matters (NOM) on TC degradation (Fig. S20 in Supporting information). The synergistic system still maintains a high degradation efficiency as the concentration of HA increases, suggesting the efficient and stable catalytic process. The cycle experiment in Fig. S21 (Supporting information) shows the removal efficiency of TC maintained at about 95.2% in fifth recycling, manifesting the acceptable stability and reusability of a-MoS_x. The concentration of Mo ions dissolved in the solution was measured after the synergistic degradation under the optimized condition. Notably, the dissolved Mo and S of 1T/2H MoS_2 are 4.2 mg/L and 10.8 mg/L, while those of a-MoS_x are 0.8 mg/L and 8.4 mg/L, respectively (Fig. S22 in Supporting information). The results indicate that a-MoS_x with 3D layer-by-layer superstructure has great stability and will not produce noteworthy metal pollution. When applied in different water environments (Longzi lake, Xiliu lake and Yellow river), the removal efficiency of TC in 60 min still reached over 80.6% (Fig. S23 in Supporting information). For the degradation of other organic pollutants, such as TC, norfloxacin (NOR) and bisphenol A (BPA), a-MoS_x also exhibits excellent synergistic adsorption and catalytic degradation performance (Fig. S24 in Supporting information). The COD removal efficiency of TC, NOR and BPA solutions reached 78.9%, 61.2%, 64.1% within 60 min, respectively (Fig. S25 in Supporting information). Raman patterns of a-MoS_x before and after catalyzing TC degradation (Fig. S26 in Supporting information) display no remarkable change, further confirming its outstanding stability.

In summary, a-MoS_x with 3D layer-by-layer superstructure formed by assembling $[Mo_3S_{13}]^{2-}$ clusters was designed and prepared. The unique structure with large interlayer spacing and abundant active sites endows a-MoS_x to have an excellent adsorption capacity to TC (106.91 mg/g). As a result, the TC degradation efficiency reached 96.6% within 20 min in the synergistic system. Various characterizations and DFT calculations were used to explore the mechanism of adsorption and PMS activation by a-MoS_x. The quenching experiments and EPR analysis discovered that $^1O_2$ and $O_2^{\bullet-}$ play the dominatant role while $^{\bullet}OH$ and $SO_4^{\bullet-}$ have a minor role in synergistic system. Furthermore, the degradation pathway of TC was explored by HPLC–MS. Meanwhile, the synergy system exhibits great potential in piratical application and the COD removal efficiency of TC solution could reach 78.9% in 60 min. This study provides ideas for catalyst design with outstanding synergistic adsorption and photo-assistant PMS activation in environment remediation.

Declaration of competing interest

The authors declare that they have no known competing financial interests or personal relationships that could have appeared to influence the work reported in this paper.

Acknowledgments

This work was financially supported by the National Natural Science Foundation of China (Nos. 52370073, 12274115), Program for Science and Technology Innovation Team in Universities of Henan Province (No. 24IRTSTHN017), Natural Science Foundation of Henan Province (No. 212300410336), Program for Science and Technology Innovation Talent in Universities of Henan Province (No. 23HASTIT027), Key Scientific and Technological Project of Henan Province (No. 222102320188), Key Project of Science and Technology Research of Henan Provincial Department of Education (No. 21A430008).

Supplementary materials

Supplementary material associated with this article can be found, in the online version, at doi:10.1016/j.cclet.2024.109764.

References

[1] Y. Li, B. Yu, B. Liu, et al., Chem. Eng. J. 452 (2023) 139542.
[2] T. Liu, Y. Li, H. Sun, et al., Chin. J. Struct. Chem. 41 (2022) 2206055.
[3] A. Mei, W. Chen, Z. Yang, et al., Angew. Chem. Int. Ed. 62 (2023) e202301440.
[4] T. Wang, J. He, J. Lu, et al., Chin. Chem. Lett. 33 (2022) 3585–3593.
[5] P. Muang-Non, C. Richardson, N.G. White, Angew. Chem. Int. Ed. 62 (2023) e202212962.
[6] J. Song, N. Hou, X. Liu, et al., Adv. Mater. 35 (2023) 2209552.
[7] J. Yang, M. Zhang, M. Chen, et al., Adv. Mater. 35 (2023) 2209885.
[8] M. Wang, F. Wang, P. Wang, et al., Sep. Purif. Technol. 326 (2023) 124806.
[9] F. Wang, Y. Gao, H. Chu, et al., ACS ES&T Eng. 4 (2024) 153–165.
[10] Z.C. Zhang, F.X. Wang, C.C. Wang, et al., Sep. Purif. Technol. 327 (2023) 124944.
[11] X. Zhang, J. Zhang, B. Hou, et al., Appl. Surf. Sci. 643 (2024) 158663.
[12] J. Yu, X. Li, Z. Jin, et al., Chin. J. Struct. Chem. 41 (2022) 2206001–2206002.
[13] Y. Guo, C. Xin, L. Dai, et al., Sep. Purif. Technol. 284 (2022) 120297.
[14] Q. Tang, W. Tu, Y. Zhou, et al., Chin. J. Struct. Chem. 42 (2023) 100170.
[15] X. Yu, C. Zhou, Z. Huang, et al., Appl. Catal. B 325 (2023) 122308.
[16] S. Li, C. Wang, K. Dong, et al., Chin. J. Catal. 51 (2023) 101–112.
[17] H. Fang, J. Gao, J. Wang, et al., Sep. Purif. Technol. 314 (2023) 123565.
[18] S. Li, X. Chen, M. Li, et al., Chem. Eng. J. 441 (2022) 136006.
[19] X. Su, Y. Guo, L. Yan, et al., Sep. Purif. Technol. 282 (2022) 120118.
[20] C. Gu, T. Sun, Z. Wang, et al., Small Methods 7 (2023) 2201529.
[21] D. Wang, H. Li, N. Du, et al., Chem. Eng. J. 398 (2020) 125685.
[22] J. Chen, Z. Chen, W. Zhao, et al., Inorg. Chem. Commun. 152 (2023) 110657.
[23] X. Hua, H. Chen, C. Rong, et al., J. Hazard. Mater. 448 (2023) 130951.
[24] J. Zhu, Y. Ma, X. Chen, et al., J. Water Process Eng. 49 (2022) 103089.
[25] Z. Zeng, S. Ye, H. Wu, et al., Sci. Total Environ. 648 (2019) 206–217.
[26] X. Yang, L. Wen, H. Huang, et al., Solid. State Sci. 133 (2022) 107014.
[27] S. Ye, M. Yan, X. Tan, et al., Appl. Catal. B 250 (2019) 78–88.
[28] S. Li, W. Huang, P. Yang, et al., Sci. Total Environ. 754 (2021) 141925.
[29] L. Wang, X. Zheng, L. Yan, et al., Sep. Purif. Technol. 317 (2023) 123907.
[30] M. Huang, X. Wang, C. Liu, et al., J. Hazard. Mater. 404 (2021) 124175.
[31] Z.H. Xie, C.S. He, Y.L. He, et al., Water. Res. 232 (2023) 119666.
[32] W. Liu, Y. Lu, Y. Dong, et al., Chem. Eng. J. 466 (2023) 143161.
[33] J. Yao, N. Wu, X. Tang, et al., Chem. Eng. J. Adv. 12 (2022) 100378.
[34] Z. Chen, Z. Wei, L. Yang, et al., Chem. Eng. J. 475 (2023) 146236.
[35] Y. Li, B. Yu, H. Li, et al., Chin. Chem. Lett. 34 (2023) 107874.
[36] C. Xin, B. Wang, J. Yang, et al., Ceram. Int. 49 (2023) 37861–37871.

[37] Z. Chen, G. Liu, S. Yu, et al., Chem. Eng. J. 474 (2023) 145581.
[38] T. Ying, W. Liu, L. Yang, et al., Sep. Purif. Technol. 330 (2024) 125272.
[39] M. Cai, Y. Liu, K. Dong, et al., Chin. J. Catal. 52 (2023) 239–251.
[40] S. Zhang, G. Hu, M. Chen, et al., Appl. Catal. B 330 (2023) 122584.
[41] A. Wang, J. Ni, W. Wang, et al., Appl. Catal. B 319 (2022) 121926.
[42] L. Xie, L. Wang, X. Liu, et al., Angew. Chem. Int. Ed. (2023), doi:10.1002/anie.202316306.
[43] S. Li, K. Dong, M. Cai, et al., eScience 4 (2024) 100208.
[44] P. Gao, Z. Li, L. Feng, et al., Chem. Eng. J. 429 (2022) 132398.
[45] Q. Si, W. Guo, H. Wang, et al., Appl. Catal. B 299 (2021) 120694.
[46] X. Ge, G. Meng, B. Liu, J. Mol. Liq. 364 (2022) 120078.